Photometric Evolution of Galaxies in Cosmological Scenarios

Gertrud Contardo[1,2], Matthias Steinmetz[1,3], and Uta Fritze-von Alvensleben[4]
gcontard@eso.org, msteinmetz@as.arizona.edu, ufritze@uni-sw.gwdg.de

ABSTRACT

The photometric evolution of galaxies in a hierarchically clustering universe is investigated. The study is based on high resolution numerical simulations which include the effects of gas dynamics, shock heating, radiative cooling and a heuristic star formation scheme. The outcome of the simulations is convolved with photometric models which enables us to predict the appearance of galaxies in the broad band colors U, B, V, R, I and K. We demonstrate the effect of the mutual interplay of the hierarchical build-up of galaxies, photometric evolution, k-correction, and intervening absorption on the appearance of forming disk galaxies at redshift one to three. We also discuss to what extend the numerical resolution of current computer simulations is sufficient to make quantitative predictions on surface density profiles and color gradients.

Subject headings: cosmology: theory – galaxies: formation, evolution – methods: numerical

[1]Max-Planck-Institut für Astrophysik, Postfach 1523, 85740 Garching, Germany
[2]Present address: European Southern Observatory, Karl-Schwarzschild-Str. 2, 85748 Garching, Germany
[3]Steward Observatory, University of Arizona, Tucson, AZ 85721, USA
[4]Universitätssternwarte Göttingen, Geismarlandstraße 11, 37083 Göttingen, Germany

1. Introduction

Over the past few years, the advent of a new generation of large telescopes and the superb imaging quality of the refurbished Hubble-Space-Telescope have changed the way we can look at the formation and evolution of galaxies. Galaxies are routinely identified at redshift $z \approx 1$ and also objects at redshifts $z \approx 3$ have been optically resolved (Steidel et al. 1996). Theoretical work has been guided by the hierarchical clustering hypothesis. In this scenario, the *Cold Dark Matter* (CDM) model is probably the best known example, structures form as halos of progressively larger mass merge, virialize and form new higher mass objects. Thus, the galaxy formation process can be modeled from ab-initio conditions and model predictions can be rigorously compared to observational data. Two complementary techniques have been shown to be especially powerful.

In so-called semi-analytical studies (Kauffmann, White, & Guiderdoni 1993; Cole et al. 1994), phenomenological recipes are used to model the accumulation of gas at the center of dark matter halos and its transformation into stars. The involved free parameters are calibrated by matching present day properties of galaxies, e.g., the properties of the Milky Way or the Tully-Fisher relation. These techniques are comparably cheap as far as computation is concerned and thus allow a large coverage of the parameter space. The major strength of the semi-analytical approach lies in modeling statistical properties of the whole galaxy population as, e.g., the luminosity function of galaxies. Its disadvantage is that little can be said on details of the galaxy formation process or the exact structure and kinematics of galaxies.

Numerical hydrodynamical simulations which follow the formation of individual galaxies in detail fill in that gap. Indeed, advanced numerical simulations include all the relevant physical processes: gravitation, gas dynamics, adiabatic heating and cooling, hydrodynamic shocks, radiative cooling and star formation (Katz 1992; Navarro & White 1993; Steinmetz & Müller 1994, 1995; Evrard, Summers, & Davis 1994; Tissera, Lambas, & Abadi 1997). However, the required numerical resolution (≈ 1 kpc) together with the demanding numerical algorithms and the limited computational power of the present generation of supercomputers constrain current simulations to small box sizes, i.e., each simulation only creates very few galaxies. Thus hydrodynamical simulations can deal with the details of the galaxy formation process, but can make only limited predictions on statistical properties.

Numerical simulations have also helped identifying some of the major problems of the hierarchical clustering hypothesis: Since cooling times scale inversely with density, the dissipative collapse of gas should have been more efficient at high redshift because the dark matter halos present at that time were denser, as was the universe as a whole. Thus gas cools and settles into rotationally supported disks already when the first level of the hierarchy collapses. Consequently, models predict an overabundance of low mass galaxies as well as disk galaxies which for a given circular velocity are too massive (White & Rees 1978). A related problem is the size of present day disk galaxies: Due to the frequent merging angular momentum is efficiently transported from the baryons to the dark-matter halo resulting in disk galaxies which are too concentrated compared to present day disk galaxies (Navarro, Frenk, & White 1995; Navarro & Steinmetz 1997). Feedback processes due to star formation, like stellar winds or supernovae, have repeatedly been envisioned to solve this overcooling problem (e.g., Dekel & Silk 1986). However, a simulation which includes the effect of star formation *and* which is consistent with observations has not been performed yet.

In this paper we merge the approach of numerical simulations with traditional methods of spectrophotometric synthesis. This hybrid scheme enables us to perform an even more realistic comparison between model predictions and actual observations. The structure of the paper is the following: In section 2 details of the numerical simulations and the star formation scheme are provided and the spectrophotometric modeling is presented. In section 3 we apply these methods to model the appearance of high redshift galaxies as they form in CDM like universes. In section 4 we describe to what extend current simulations may even allow us to analyze the detailed structure of galaxies at high and low redshift. Section 5 summarizes the results and draws our conclusions.

2. Methods

2.1. Numerical simulations

The simulations were performed using Grape-SPH (Steinmetz 1996), a hybrid scheme of a smoothed particle hydrodynamics (SPH) approach with a direct summation N-body routine which uses the hardware N-body integrator GRAPE. The code is specially designed to follow a three component system of gas, stars, and dark matter and has high resolution in space and time due to the use of individual smoothing lengths and time steps. It includes the effects of pressure gradients, adiabatic heating and cooling, shocks and radiative cooling.

In the simulations presented here, a star formation scheme similar to the one in Steinmetz & Müller (1994, 1995, henceforth SM1 and SM2; see also Katz 1992) is used: Star formation is modeled by creating new collisionless "star particles" in regions where the gas is locally Jeans unstable and where the cooling timescale is shorter than the local dynamical time scale. The orbits of these newly formed star particles are subsequently followed in a self-consistent fashion, assuming that they are only affected by gravitational forces. Young star particles devolve energy and metal enriched mass to their surrounding gas, an effect that mimics the energy and mass input by supernovae and evolving stars into the ISM. The supernova energy is added to the thermal energy of the surrounding gas. Input in kinetic energy (Navarro & White 1993) is not directly implemented but is described by an efficiency parameter which is of the order of a few per cent, an assumption that is justified since we preferably concentrate on the formation of luminous galaxies like the Milky Way.

2.2. Initial conditions

We use idealized initial conditions as proposed by Katz (1991) and discussed in more detail in SM2: We consider an isolated sphere on which small scale fluctuations according to a CDM power spectrum are superimposed. To incorporate the effects of fluctuations with longer wavelengths, the density of the sphere has been enhanced and rigid rotation corresponding to a spin parameter of $\lambda = 0.08$ has been added. The simulation is identical to that presented in SM1 and SM2 where a disk galaxy similar to the Milky Way forms. These idealized initial conditions are fairly realistic for the early formation epochs ($z > 2$) when the sphere itself has not yet collapsed. The late formation epoch, however, is dominated by the collapse of the sphere and hence proceeds more smoothly than under more realistic conditions. Due to the smooth infall at low redshifts the simulation does not suffer from the angular momentum problem. Furthermore, this model allows for very high numerical resolution (spatial resolution 1 kpc, mass resolution $10^7\,\mathrm{M}_\odot$) at comparably low computational cost.

2.3. Simulation outcome

At any redshift, the simulations provide the spatial distribution of star particles. Each star particle corresponds to a population of about one million stars which have formed in a burst, i.e., the whole galaxy is a superposition of several ten thousands of mini starbursts. Each of the star particles is described by its age (time passed since creation) and its metallicity.

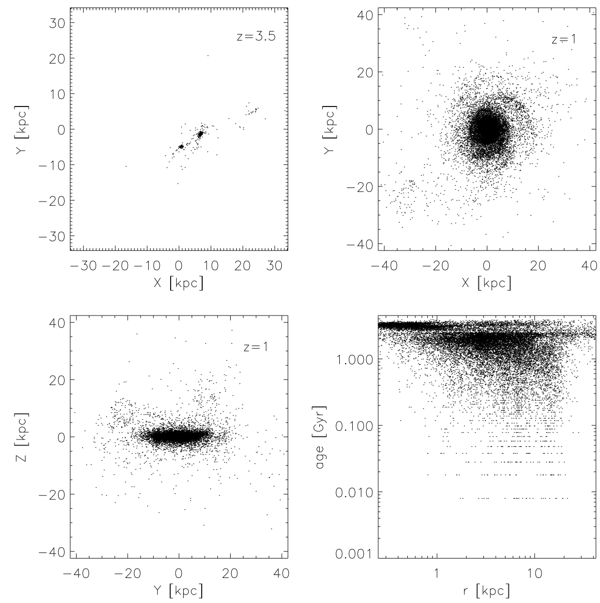

Fig. 1.— Upper left: distribution of star particles at redshift $z = 3.5$. The sidelength of the plots corresponds to 100 pixels of the HST/WFPC2. Upper right: face-on view of the galaxy at redshift $z = 1$. Lower left: edge-on view of the galaxy at redshift $z = 1$. Lower right: age of star particles at $z = 1$ as a function of their distance to the galaxy center.

The actual distribution of star particles is shown in figure 1. Details on the formation history of the model galaxy, of its kinematical properties as well as of its chemical evolution can be found in SM1 and SM2. Here we concentrate on some features important for the discussion later in this paper. At redshift 3.5, two protogalactic clumps can be seen which are going to merge within the following $\approx 10^8$ years. At lower redshifts, the stars originating in these two clumps can be found in the bulge of the galaxy. At $z = 1$, the model galaxy already resembles a Milky Way type galaxy with a bulge-to-disk ratio of 1:3 in mass (SM2). In the lower right panel of figure 1, we plot the age of the star particles as a function of the distance to the galaxy center. The central 1-2 kpc are dominated by old stars with an age between 3 and 4 Gyr. The majority of these star particles has a metallicity of above solar (SM1). There is little offset between the age of the oldest stars (3.9 Gyr) and the age of the universe at that redshift (4.6 Gyr). This feature is common to any hierarchically clustering universe in which the first stars form in small clumps which collapse at high redshifts. The actual value here is only an upper limit since (i) the limited numerical resolution cannot follow star formation in clumps with less than $\approx 10^6\,\mathrm{M}_\odot$ and (ii) the amount of substructure is underrepresented due to the idealized initial conditions. At larger radii ($r > 2$ kpc), younger stars with an age of about 1 Gyr and below are dominating which reflects ongoing star formation in the gaseous disk. Due to the vacuum boundary conditions, the evolution of the galaxy is fairly quiescent at redshifts below one. Gas in the disk is successively transformed into stars. Due to the still insufficient numerical resolution, however, encounters between disk stars and dark matter particles act as a kinematic heating term. While at $z = 1$ the velocity dispersion of disk stars is still small (≈ 10 km/sec), the stellar disk is successively heated up between $z = 1$ and $z = 0$ up to velocity dispersions near 100 km/sec at $z = 0$ (SM2, see also Steinmetz & White 1997). We therefore focus our analysis mainly on redshift one, when the amount of artificial heating is still negligible.

2.4. Spectral synthesis

As mentioned above, each star particle, which has a typical mass of a few million solar masses, corresponds to a population of several million stars which have been formed at the same time t_f from a gas cloud with a metallicity of Z. A star particle can thus be considered as a population of stars which have formed in a burst-like manner. The luminosity evolution of such a burst is then followed by an evolutionary spectral synthesis model (Fritze-von Alvensleben & Gerhard 1994; Fritze-von Alvensleben & Burkert 1995; Einsel et al. 1995): The evolution of this instantaneously formed population of stars is followed in the Hertzsprung–Russell diagram (HRD) using results of stellar evolution theory. Sets of stellar tracks (Maeder 1990) for five different metallicities ($Z = 10^{-4}$, 10^{-3}, 4×10^{-4}, 10^{-2}, 4×10^{-2}) and for 27 stellar masses in the range of $0.15\,\mathrm{M}_\odot$ to $60\,\mathrm{M}_\odot$ have been compiled by Einsel et al. (1995). A Miller-Scalo (1979) initial mass function (IMF) is assumed with upper and lower mass limits of $60\,\mathrm{M}_\odot$ and $0.15\,\mathrm{M}_\odot$, respectively. The spectrum of an individual star burst is synthesized from Kurucz's (1992) library of stellar spectra, luminosities in various filter bands are obtained by convolution with filter response functions (see also Leitherer et al. 1996, Fritze-von Alvensleben & Kurth 1996).

The discrete set of stellar masses for which stellar evolution tracks are available together with the burst-like star formation history can cause some problems for the late time evolution of the population. In the original implementation, all stars within a mass interval $\left[m_{i-1/2}; m_{i+1/2}\right]$ have been assigned to the temperature and luminosity of the stellar track of a star of mass m_i. For masses below $2\,\mathrm{M}_\odot$, the lifetime on the red giant branch (a few $10^8\,$yr) is, however, short compared to the difference in the lifetime of stars on neighboring evolutionary tracks ($10^9\,$yr). This causes all stars within a given mass interval to synchronously enter the red giant branch. Since the luminosity increases hundredfold, and since every mass interval contains a substantial fraction of the total mass of the population (a few per cent), pronounced spikes in the luminosity can be seen (figure 2, dotted line). Such a discreteness dominated behavior is unknown for extended star formation histories (as e.g. in models of spiral galaxies), since these spikes are convolved (and thus smoothed) with the star formation history.

These discreteness effects in the luminosity evolution of burst-like formed populations are circumvented by methods which are based on isochrones (see, e.g., Bruzual & Charlot 1993).

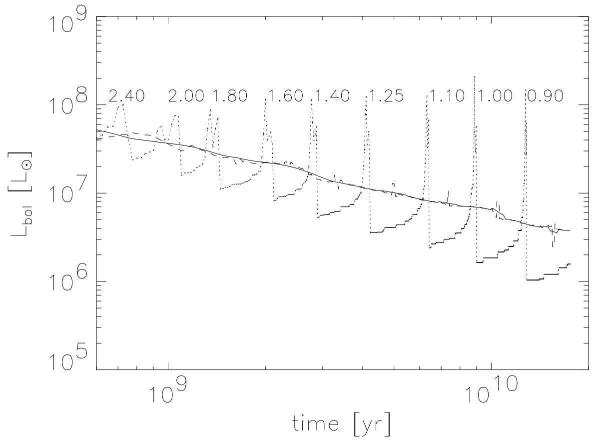

Fig. 2.— Luminosity evolution of a stellar population formed within 2.5×10^7 years with metallicity $Z = 1\times10^{-4}$. The dotted line shows the evolution as computed with the original code. The luminosity indicated by the dashed line is calculated with the averaged stellar evolution tracks and smoothed subsequently (solid line). The numbers right of the peaks assign the mass m_i in $\mathrm{M}_\odot$ of the star that reaches the red giant branch at that time.

We propose an alternative method that avoids the construction of isochrones. The luminosity evolution of an individual star is split into two parts, main sequence and post main sequence. As can be seen in figure 3, the post main sequence evolution between neighboring masses is almost identical, concerning the time dependence as well as the luminosity evolution. The main sequence evolution $l_{\mathrm{MS}}\left(t,m\right)$ has also a very similar shape, but the evolution is faster for the higher masses and the star is also brighter. These two effects can, however, be compensated by the following ansatz for the luminosity evolution of a star with mass $m + \Delta m$:

$$l_{\mathrm{MS}}\left(t, m+\Delta m\right) = l_{\mathrm{MS}}\left(t', m\right)\,\left(\frac{m+\Delta m}{m}\right)^{\alpha}. \qquad (1)$$

In this ansatz, α is the exponent of the mass-luminosity relation, typical values being $\alpha \approx 3$

for masses less than a few $\mathrm{M}_\odot$. The rescaled time t' can be inferred by rescaling t with the ratio of the life times on the main sequence τ_{MS}, i.e.,

$$t' = t\,\frac{\tau_{\mathrm{MS}}\,(m+\Delta m)}{\tau_{\mathrm{MS}}\,(m)} = t\,\left(\frac{m+\Delta m}{m}\right)^{\beta} \qquad (2)$$

with $\beta \approx -2$; stars with a higher mass reach a given evolutionary stage faster. For each mass m within the mass interval $\left[m_{i-1/2}; m_{i+1/2}\right]$ the luminosity evolution can thus be calculated. The local value of the slope of the mass-luminosity and mass-lifetime relation, α and β, can be drawn from neighboring masses m_i. In figure 3 we demonstrate the success of our interpolation scheme by comparing the evolution of a star of mass $M = 1.6\,\mathrm{M}_\odot$ with the evolution as inferred from a star with $M = 1.4\,\mathrm{M}_\odot$ and $M = 1.8\,\mathrm{M}_\odot$ using the interpolation scheme above. Differences in the main sequence evolution are almost undetectable and also the post main sequence evolution differs only by a very small time shift (less than 10 per cent of the lifetime on the post-main-sequence).

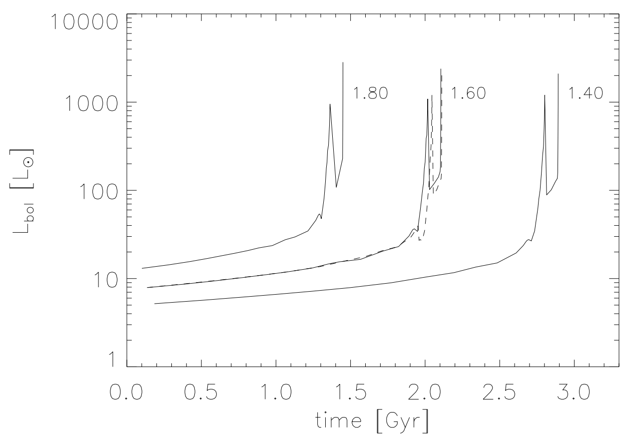

Fig. 3.— Comparison of the luminosity evolution of three stars of mass $M = 1.4\,\mathrm{M}_\odot$, $1.6\,\mathrm{M}_\odot$ and $1.8\,\mathrm{M}_\odot$, respectively. The dashed line has been obtained by interpolating between the $M = 1.4\,\mathrm{M}_\odot$ and $1.8\,\mathrm{M}_\odot$ track as described in the text.

By averaging these approximated stellar evolution tracks in each mass interval and by adding up the luminosities according to the initial mass function (IMF) the total luminosity of the stellar population is obtained as a function of time. The luminosity of populations which formed in a single star burst now evolves much smoother (see figure 2, dashed line). The remaining small wiggles result from discontinuities in the evolution near the interface of two adjacent mass intervals. We remove these wiggles by averaging over time intervals of 1.5×10^8 years, as indicated by the solid line in figure 2.

The luminosity evolution in the U and K band of a single star burst is shown for 5 different metallicities in figure 4. Data for arbitrary metallicities Z can then be obtained by interpolation in $\log Z$.

2.5. k correction

For apparent magnitudes and colors of galaxies at high redshifts the modifications due to the redshift of the spectrum have to be taken into account.

The cosmological redshift causes the spectral energy distribution $F_0\,(\lambda)$ of a galaxy in its restframe at redshift z_r to be detected in the observers restframe as $F\,(\lambda)$ with:

$$F\,(\lambda, z_r) \;=\; \frac{F_0\,(\lambda/(1+z_r))}{(1+z_r)}. \qquad (3)$$

The apparent magnitude in some "X" filter band is thus

$$m_X = BDM\,(z_r) - 2.5\log\left(\frac{L_{X0}}{\mathrm{L}_{\mathrm{X}\odot}}\right) + \mathrm{M}_{\mathrm{X}\odot} + \mathrm{k}\,(\mathrm{z_r})\,. \qquad (4)$$

with the luminosity L_{X0} in the galaxy's rest frame, the bolometric distance modulus

$$BDM\,(z_r) = 5\log\left(D_L\,(z_r)/\mathrm{Mpc}\right) + 25,$$

and the luminosity distance (Mattig 1958)

$$\begin{aligned} D_L\,(z_r) \;&=\; \frac{c}{H_0 q_0^2}\left\{z_r q_0 + (q_0 - 1)\right. \\ &\qquad \left.\times\left[-1 + \sqrt{(2q_0 z_r + 1)}\right]\right\}. \end{aligned} \qquad (5)$$

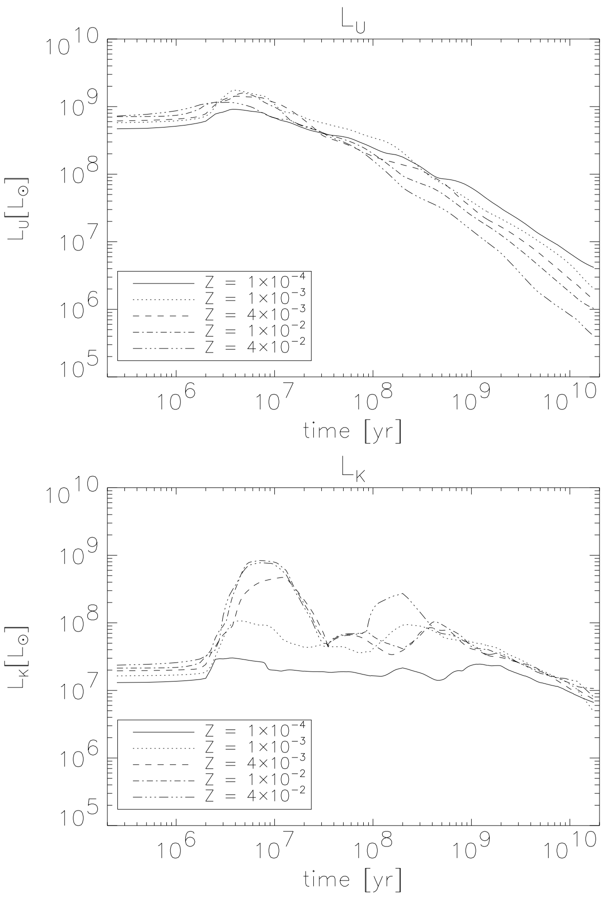

Fig. 4.— Luminosity evolution in the U and K band of a single age stellar population for the metallicities $Z = 1\times10^{-4}, 1\times10^{-3}, 4\times10^{-3}, 1\times10^{-2}$, and 4×10^{-2}. The total mass of the population is $1\times10^{7}\,\mathrm{M}_\odot$.

The *k correction* is calculated from the spectral energy distribution $F(\lambda)$ and the filter response function $S_X(\lambda)$ (Lamla 1982) according to the following equation (Oke & Sandage 1968)

$$k = -2.5\log\left(L_{X\,\mathrm{Obs.}}/L_{X0}\right) \quad (6)$$

$$= 2.5\log\frac{(1+z_r)\int_0^\infty F_0(\lambda)\,S_X(\lambda)\,d\lambda}{\int_0^\infty F_0(\lambda/(1+z_r))\,S_X(\lambda)\,d\lambda} \quad (7)$$

2.6. Creating artificial images

From the luminosity of the set of star particles, artificial images can be easily generated. The luminosity in a given pass band filter can be converted into number of photons emitted per unit time per solid angle. This number is corrected by intervening absorption due to neutral hydrogen using the models of Madau (1995). By specifying exposure time and pixel size, the number of photons received by each pixel is calculated. The pixel map then is convolved with the numerical resolution of the simulation and the sky background is added. Finally it is convolved with the point-spread function of the instrument. The resulting array contains the expectation value for each pixel to receive a photon. This number is then random-sampled. Together with the detector characteristics (quantum efficiency, readout noise, dark current, gain) an artificial image can be created which subsequently can be analyzed in the same way as raw observational data.

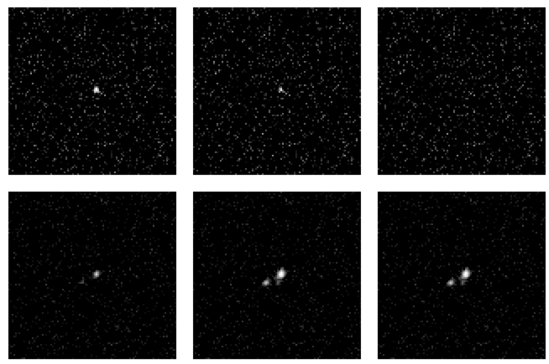

Fig. 5.— Artificial HST images of a forming galaxy at $z = 3.5$. Images are 50 pixels across, "exposure time" is 30000 sec. Top row: U-band; bottom row: I-band. Left column: rest frame; middle column: including k-correction; right column: including k-correction and absorption due to intervening hydrogen.

3. Applications

3.1. Appearance of high redshift galaxies

In this paragraph we discuss the appearance of the simulated galaxies in an exposure as it is typical for HST/WFPC2 observations. De-

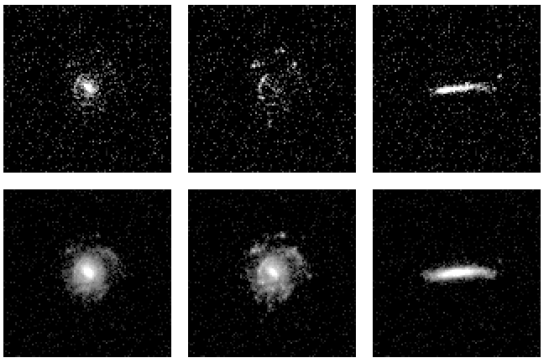

Fig. 6.— Artificial HST images of a forming galaxy at $z = 1$. Images are 50 pixels across, "exposure time" is 30000 sec. Top row: U-band; bottom row: I-band. Left column: face on, rest frame; middle column: face on, including k-correction; right column: edge-on, including k-correction

tector characteristics and sky background have been taken from the WFPC2 handbook and a generous exposure time of 30000 s has been specified. For the adopted cosmological model ($\Omega = 1$, $H_0 = 50\,\mathrm{km\,s^{-1}\,Mpc^{-1}}$) and redshift range ($z = 1-4$), the formal numerical resolution of the simulation surpasses the pixel resolution of the WFPC2 camera by about 50%.

In figure 5 and 6 we show a U and I-band image of the simulated galaxy at redshifts $z = 1$ and $z = 3.5$. Each image has a side length of 100 pixels, corresponding to 70 kpc ($z = 3.5$) and 82 kpc ($z = 1$), respectively. Grayscales have been chosen logarithmically to cover the interval between a signal-to-noise of 1 to 30 (U band) and 100 (I band).

In the restframe U-band image of the z=3.5 galaxy, only the most massive clump is visible. It has an apparent magnitude of $m_U = 24.8$. Applying the k-correction makes the clump barely visible ($m_U = 25.7$). At these redshifts, the U-band is centered at wavelengths shortward of 912 Å in the galaxy's restframe where stellar emission is depleted due to absorption in the stellar atmosphere. Absorption due to inter-

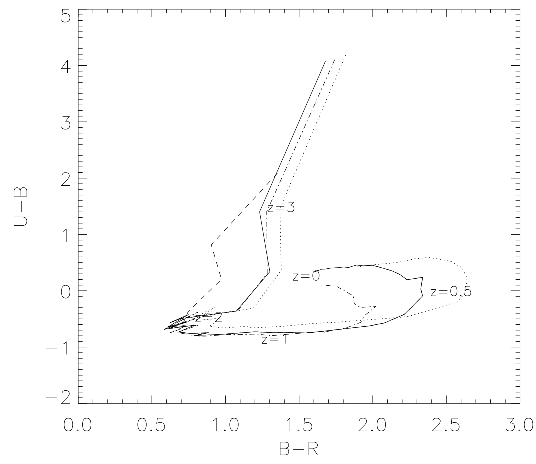

Fig. 7.— Evolution of the model galaxy in the $U-B$ vs. $V-R$ plane. Solid line: model galaxy, including k-correction and intervening absorption; dashed line: model galaxy, k-corrected, no absorption; dotted line: E galaxy; dashed-dotted: Sd galaxy (from Möller, Fritze-von Alvensleben, & Fricke 1997).

vening neutral hydrogen suppresses the U-band emission of the proto galaxy by further 3.5 mag ($m_U = 29.2$) and makes it invisible even in long exposures.

In the I-band, the k-correction has the opposite effect: in its restframe, the apparent magnitude is $m_I = 24.6$ and also the less luminous progenitor is barely visible. The luminosity of the galaxy is dominated by stars which have formed within the last few 10^8 yr and also massive stars $M > 8\,\mathrm{M_\odot}$ are abundant. Thus, these lumps strongly emit in the near UV (≈ 4000 Å). The cosmic redshift translates these frequencies to the I-band resulting in a negative k-correction of 1.7 magnitudes ($m_I = 22.9$). The galaxy thus has a brightness compatible to the brightest galaxies in the Steidel et al. (1996) sample. Since at $z = 3.5$ the I-band corresponds to wavelengths longward of 1217 Å, the luminosity is not affected by intervening absorption.

The restframe U-band image of the $z = 1$ galaxy consists of a luminous bulge of stars with a typical age of $3 - 4\,$Gyrs (see figure 1, lower right panel) and some light from star forming regions in the disk. At redshift 1, however, the U-band corresponds to restframe wavelengths near 1800 Å where the emission of old stars is small. Thus the bulge component virtually disappears after applying the k-correction. Similar to the $z = 3.5$ I-band, k-correction enhances the star forming regions in the disk. Young massive stars emit strongly at restframe wavelengths near 2000 Å which are redshifted into the U-band. Similar effects can be seen in the I-band image: Since the I-band corresponds to a restframe wavelength of 4000 Å, also the light of the old bulge component is clearly visible, although slightly dimmed. For the disk population the k-correction favors shorter wavelengths at which the contribution of newly formed stars is larger. Consequently, the k-corrected I-band image looks more structured and the regions of active star formation are more pronounced.

In figure 7 the evolution of the model galaxy in the $U-B$ vs. $B-R$ plane is shown and, for comparison, the evolution of a Sa and Sd galaxy using traditional spectrophotometric models (see, e.g., Bruzual & Charlot 1993, Möller et al. 1997) is plotted.

3.2. Surface brightness, color gradients

In figure 8 we show surface brightness profiles and color gradients. The radial profile clearly shows an exponential behavior for $r > 5\,$kpc and a steepening (bulge) at smaller radii. The non-exponential bulge component is readily visible in the $z = 0$ plot since the surface brightness of the disk has dimmed by about one magnitude. A comparison of the k-corrected (figure 8 top) galaxy at $z = 1$ with its restframe (figure 8 middle) exhibits a substantial (slight) enhancement of the K (I) luminosity (i.e., the k-correction is negative), while the V and U luminosity is dimmed.

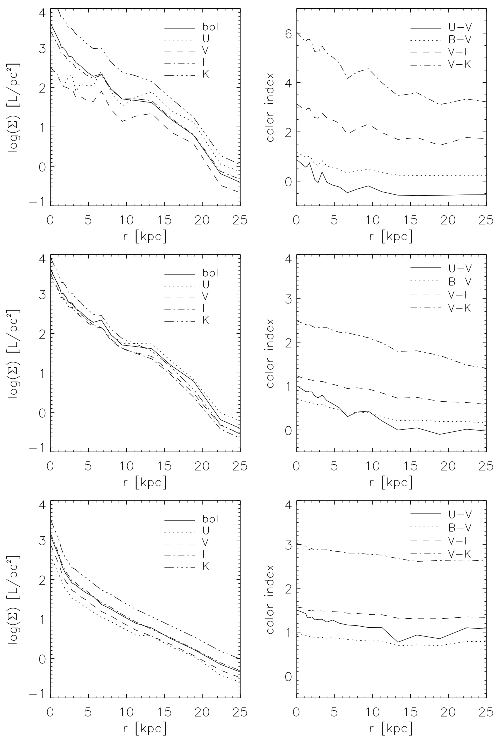

Fig. 8.— Left column: Surface density versus radius. The solid line corresponds to the bolometric luminosity, the dashed, dotted, dashed-dotted and dashed-triple-dotted line correspond to the broadband colors U, V, I and K, respectively. Right column: color indices $U-V$(solid), $B-V$(dotted), $V-I$(dashed) and $V-K$(dashed-dotted) versus radius. From top to bottom: $z = 1$ including k-correction, $z = 1$ restframe and $z = 0$.

At $z = 1$ the galaxy exhibits very strong reddening within the inner 5 kpc, about 2 magnitudes in $V-K$ and 1 magnitude in the other colors. Except $U-V$, the drop is much weaker in the restframe. This reddening is consistent with the dimming of the bulge component of the $z = 1$ galaxy due to k-correction as described in section 3.1. The bulge is dominated by old stars (see figure 1, lower right panel) emitting only little near 1800 Å which corresponds to the U band at $z \approx 1$. The k-correction enhances the K and I luminosity while decreasing the U and V luminosities and thus results in the strong reddening as can be seen in figure 8. Only a slight color gradient is visible at radii $r > 10\,\mathrm{kpc}$ in the rest-frame as well as in the k-corrected profile. Also the effect of the k-correction is much more moderate, between 0 mag in $B-V$, 0.6 mag in $U-V$ and 1.5 mag in $V-K$. At these radii, stars are still being formed resulting in a much flatter spectral energy distribution and thus a much weaker k-correction.

At $z = 0$, only very weak color gradients are visible. The bulge differs from the disk by about 0.1 mag, only in $U-V$ a slightly stronger color gradient is visible. The change of color is certainly much weaker than the observed one of about 0.2 mag in $B-V$ and 0.5 mag in $U-V$ as in galaxies like, e.g., Andromeda (Segalovitz 1975; Josey & Arimoto 1992). One reason for this discrepancy is the neglect of dust absorption. As we will show in the next paragraph, however, the lack of significant color gradients may also be an artifact of our star formation scheme and of the vacuum boundary conditions.

In figure 9 we investigate to what extend the color gradients at $z = 1$ and $z = 0$ reflect age and metallicity gradients of the stellar disk. First we estimate the statistical error of the color indices. For that purpose we perform a bootstrap analysis, i.e., we draw 100 random samples from the distribution of stars and determine color as a function of radius. We use the [10; 90] percentile values as the lower and upper error limits, i.e., only 10% of our bootstrapped samples have a color bluer than our lower error limit and only 10% of our bootstrapped samples have a color redwards of our upper limit. As can be seen, colors can be measured with a statistical error of about ± 0.02 to 0.05 mag at $z = 0$. At $z = 1$, errors are at the level of about ± 0.1 to ± 0.2. These errors strongly depend on whether or not stars are actively formed. While colors are fairly accurate for passively evolving populations, errors are much larger for regions including young stars. This can be easily seen in the $z = 0$ $U-V$

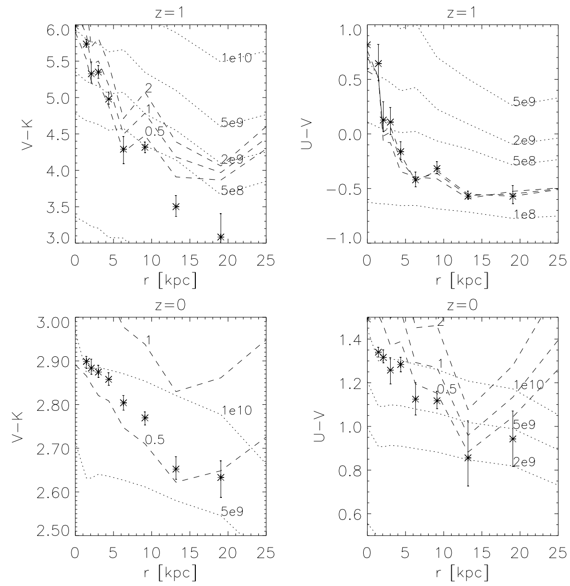

Fig. 9.— k-corrected $V-K$ (left) and $U-V$ (right) as a function of radius for the model galaxy at redshift $z = 1$ (top) and $z = 0$ (bottom). Stars correspond to the model galaxy, error bars are [10; 90] percentile values based on a bootstrap analysis (for details, see text). The dashed lines correspond to a model with constant metallicity while stellar ages are taken from the simulation. The dotted lines correspond to a model with constant stellar ages while metallicities are taken from the simulation. A comparison of the actual values with the dashed and dotted lines thus demonstrates the effect of metallicity and age on the color gradient.

color at a radius of 12 kpc. This radial bin contains very few very young stars. The color thus strongly depends on how many of these young star particles happen to be included in the bootstrapped sample.

We also compare the radial color profiles with those obtained assuming a constant metallicity for the star particles. For the $z = 1$ model the color near the center is consistent with a metallicity of $Z \approx Z_\odot$, while the color at 15 kpc requires a metallicity much below $0.5\,Z_\odot$. No constant metallicity model fits the entire color gradient.

The metallicity gradient inferred from the color is consistent with the directly measured metallicity gradient of $0.05\,\mathrm{kpc}^{-1}$. The color gradient is not consistent with the assumption of a constant age. $U-V$ near the center requires a stellar age of 3 Gyr, while at radii of 15 kpc an average age of a few 10^8 years seems to provide the best fit, being consistent with the age distribution shown in figure 1. A comparison of $U-V$ and $V-K$ also demonstrates that the age distribution at a particular radius is inconsistent with the assumption of a constant age: For example, at radii below $r = 5\,\mathrm{kpc}$ the age which fits $V-K$ is more than 2 times larger than the best fitting age for $U-V$.

At $z = 0$, this picture changes. The color gradient is consistent with a constant metallicity of about $0.5\,Z_\odot$ and only a very slight age gradient is visible. $Z = 0.5 - 1.0\,Z_\odot$ is the average metallicity of Milky Way bulge stars (McWilliam & Rich 1994), $Z = 0.5\,Z_\odot$ compares well with the stellar metallicities in Sb models of Möller et al. (1997). However, the actual metallicity gradient in this model is much weaker ($< 0.01\,\mathrm{kpc}^{-1}$). A comparison of the $z = 1$ and $z = 0$ model thus provides a further argument for the lack of a significant color gradient at $z = 0$ and the too small metallicity gradient. As shown in SM1, the model galaxy also exhibits a too large fraction of low metallicity stars (the so-called G-dwarf problem). The reason for the failure to reproduce a significant metallicity gradient can be found either in the chosen star formation law or in the vacuum boundary conditions or both. Between $z = 1$ and $z = 0$ the disk is dynamically inactive. Only gas is continuously transformed into stars. Thus each fluid element can be considered as a closed box model. The metallicity of a closed box model increases monotonically until the yield is reached. The yield is, however, identical for each fluid element since the same IMF has been used. The almost constant metallicity at $z = 0$ thus reflects the fact that the metallicity of each fluid element has already reached its asymptotic value. This artifact can be avoided by: (i) decreasing the star formation efficiency; in that case a metallicity gradient forms since the metallicity of low density gas at larger radii does not yet reach its asymptotic value; (ii) inflow of gas at redshift $z < 1$, i.e., non-vacuum boundary conditions. We argue that (ii) will be a necessary entity, not only since such a late infall is a generic prediction of any hierarchically clustering scenario, but also because it may help to cure the G-dwarf problem.

4. Discussion and conclusions

We have simulated the formation of a Milky-Way type galaxy in a hierarchically clustering scenario using idealized initial and boundary conditions. The simulation outcome has been analyzed with spectrophotometric methods. The most important results are:

1. A hybrid scheme of high resolution numerical simulations of galaxy formation and spectrophotometric modeling is presented. We demonstrated the capabilities of such an approach. In particular, we were able to model galaxies with an appearance qualitatively similar to observed galaxies at redshifts between $z = 0$ and $z = 4$. Using the appearance of $z = 1$ and $z = 3.5$ galaxies we also could nicely demonstrate the mutual interplay between the galaxy formation process, k-correction and intervening absorption.

2. The numerical resolution of present day computer simulations enables us to study the detailed structure of galaxies as a function of redshift, such as surface brightness profiles and color gradients. Numerical resolution is high enough and statistical errors are sufficiently small to infer whether a significant metallicity or age gradient of the stellar population are present.

3. The properties of a model galaxy are among others dependent on the particular star formation scheme, IMF, supernovae feedback. We are, however, optimistic, that a rigorous comparison of high-resolution numerically simulated galaxies with the vast amount of detailed observations at different redshifts may allow us to constrain and tighten the parameter space. Such an ansatz is very similar to the calibration step performed in phenomenological models. The work presented in this paper is only a very first, but necessary step into that direction.

4. Although this work is based on a single numerical simulation and a particular star formation model, it already provides some interesting physical results. The models fail to produce a significant color gradient in spiral galaxies at low redshifts and are subject to a G-dwarf problem. Both problems arise from the idealized boundary conditions, in particular the lack of any late infall of gas. Other explanations include, but are not limited to, the neglect of reddening due to dust.

This work is partially supported by the Deutsche Forschungsgemeinschaft under SFB 375-95 and 446 JAP-113/109/0. MS appreciates the hospitality at the Department of Astronomy, University of California at Berkeley, where part of this work has been performed.

REFERENCES

Bruzual, G., & Charlot, S. 1993, ApJ, 405, 538

Cole, S. M., Aragón-Salamanca, A., Frenk, C. S., Navarro, J. F., & Zepf, S. E. 1994, MNRAS, 271, 781

Dekel, A., & Silk, J. 1986, ApJ, 303, 39

Einsel, C., Fritze-von Alvensleben, U., Krüger, H., & Fricke, K. J. 1995, A&A, 296, 347

Evrard, A. E., Summers, F. J., & Davis, M. 1994, ApJ, 422, 11

Fritze-von Alvensleben, U., & Burkert, A. 1995, A&A, 300, 58

Fritze-von Alvensleben, U., & Gerhard, O. E. 1994, A&A, 285, 751

Fritze-von Alvensleben, U., & Kurth, O. 1996, AAS CD-ROM Ser. Vol. 7

Josey, S. A., & Arimoto, N. 1992, A&A, 255, 105

Katz, N. 1991, ApJ, 368, 325

Katz, N. 1992, ApJ, 391, 502

Kauffmann, G., White, S. D. M., & Guiderdoni, B. 1994, MNRAS, 264, 201

Kurucz, R. L. 1992, in IAU Symp., Vol. 149, The Stellar Populations of Galaxies, ed. B. Barbury, & A. Renzini (Dordrecht: Kluwer), 225

Leitherer, C., et al. 1996, PASP, 108, 996

Lamla, E. 1982, in Landolt-Börnstein, Vol. VI/2b, ed. K.-H. Hellwege (Berlin: Springer), 71

Madau, P. 1995, ApJ, 441, 18

Maeder, A. 1990, A&AS, 84, 139

Mattig, W. 1958, Astron. Nachr., 284, 109

McWilliam, A., & Rich, R. M. 1994, ApJS, 91, 749

Miller, G. E., & Scalo, J. M. 1979, ApJS, 41, 513

Möller, C. S., Fritze-von Alvensleben, U., & Fricke, K. J. 1997, A&A, 317, 676

Navarro, J. F., Frenk, C. S., & White, S. D. M. 1995, MNRAS, 275, 56

Navarro, J. F., & Steinmetz, M. 1997, ApJ, 478, 13

Navarro, J. F., & White, S. D. M. 1993, MNRAS, 265, 271

Oke, J. B., & Sandage, A. 1968, ApJ, 154, 21

Segalovitz, A. 1975, A&A, 40, 401

Steidel C. C., Giavalisco M., Pettini M., Dickinson M., & Adelberger K. L. 1996, ApJ, 462, L49

Steinmetz, M. 1996, MNRAS, 278, 1005

Steinmetz, M., & Müller, E. 1994, A&A, 281, L97 (SM1)

Steinmetz, M., & Müller, E. 1995, MNRAS, 276, 549 (SM2)

Steinmetz, M., & White, S. D. M. 1997, MNRAS, 288, 545

Tissera, P. B., Lambas, D. G., Abadi, M. G. 1997, MNRAS, 286, 384

White, S. D. M., & Rees, M. J. 1978, MNRAS, 183, 341

This 2-column preprint was prepared with the AAS LaTeX macros v4.0.